

A numerical and experimental study on turbulent natural convection in a differentially heated cavity

Driek Rouwenhorst
Engineering Fluid Dynamics
University of Twente
The Netherlands
d.rouwenhorst@student.utwente.nl

Florianópolis, Brazil, 03/2011 - 07/2011

Supervisor POLO: Prof. Cesar J. Deschamps
Supervisor UT: Prof. dr. ir. H.W.M. Hoeijmakers



*Report of internship activities at POLO, Research Laboratories for
Emerging Technologies in Cooling and Thermophysics.*

Abstract

The three-dimensional flow field and temperature distribution in a differentially heated vertical cavity is identified by means of different numerical models and experimental measurement techniques. Numerically, the performance of different turbulence models are validated with DNS data available in literature. The main results will be published in the XXXII Iberian Latin-American Congress on Computational Methods in Engineering (CILAMCE). A model with sufficient performance will be used to simulate the flow in the experimental setup to give an accurate description of the phenomenon. Along specific contours the velocity field is measured experimentally in two dimensions applying Laser Doppler Velocimetry (LDV). For a more global overview of the flow behavior Particle Image Velocimetry (PIV) is used in some cross-sectional planes. In addition, the temperature distribution in the flow is visualized exploiting the Liquid Crystal Thermography (LCT) measurement technique. Finally, the heat flux distribution from the heated walls to the fluid is obtained by the positioning of an array of flux sensors. The classifying Rayleigh number is defined by the height of the cavity, which is related to its square base by an aspect ratio of four. Numerically $Ra_H = 6,4 \cdot 10^8$ and 10^{10} are considered with air as working fluid ($Pr = 0.71$), making it possible to compare the results with available DNS data. In the experiments water is used ($Pr = 7.0$) and is exposed to a temperature difference such that $Ra_H = 1 \cdot 10^{10}$ is achieved, where the flow is measured with the non-intrusive techniques. The experimental results will complement existing data at lower Rayleigh numbers available in literature. The main object is to extend the availability of accurate experimental data on natural convection in differentially heated cavities. This data can be exploited to validate different numerical methods, trying to capture the behavior of turbulent natural convection in the most efficient way. The work outlined above is the graduation project of André Popinhak, in which I was assigned to assist. The activities had already begun before the internship started and was not finished before the end of this period, therefore the subjects described are representative for the learned theory and performed tasks of the internee rather than a complete description of the research carried out.

Keywords: Natural convection; Turbulence; Cavity; LDV; LCT

Contents

1	Introduction	4
2	Theory	5
2.1	Governing equations	5
2.2	Turbulence modeling	6
2.2.1	Time averaging	6
2.2.2	Closure problem	7
2.2.3	Mixing length	7
2.2.4	$k - \varepsilon$ model	7
2.2.5	Reynolds stress equation model (RSM)	8
2.2.6	Large eddy simulation (LES)	8
2.2.7	Wall treatment	8
3	Numerical simulation	10
3.1	Solution procedure	10
3.2	<i>SST</i> $k - \omega$ model	11
3.3	RSM	11
3.4	Conclusions	11
3.5	Large eddy simulation	14
3.5.1	Mesh design	14
3.5.2	Journal file	15
3.5.3	Solution procedure	15
4	Experimental setup	17
4.1	Cavity	17
4.1.1	Environment	17
4.1.2	Radiation	17
4.1.3	Thermal boundary conditions	17
4.2	Measurement instrumentation	18
4.2.1	Positioning system	18
4.2.2	LDV	18
4.2.3	PIV	18
4.2.4	LCT	18
4.2.5	Wall heat flux measurement	19
5	Laser Doppler Velocimetry	20
5.1	The optic system	20
5.2	Test measurements	21
5.2.1	half-height, low turbulence	22
5.2.2	80 percent height, high turbulence	24
6	Particle Imaging Velocimetry	27

7	Liquid Crystal Thermography	28
7.1	Camera procurement	28
7.2	Image filtering	28
7.3	Conversion to temperature	30
7.3.1	One-parameter correlation	30
7.3.2	Neural networks	31
7.4	Calibration	31
8	Heat Flux	33
9	Conclusions	34
9.1	Postscript	34
10	Appendix A	35

1 Introduction

Natural convection is a phenomenon occurring in every environment containing a fluid with temperature gradients, provided that the density is a function of the temperature. In many engineering applications the contribution of natural convection can be disregarded because often the contribution to the flow behavior is negligible when compared to forced convection. Yet there is still a variety of engineering problems concerned with natural convection, such as convection in a double glazed window, which increases heat transfer.

For convenience, research on natural convection is often carried out on rectangular enclosures, as it is a simple geometry for both the experimental and numerical approach. Several results are available for laminar natural convection in cubical enclosures with heated sides, bottom or positioned under an angle with respect to the direction of gravity. The case considered in the present research deals with heated side walls, referred to as differentially heated walls. In earlier investigations it has been found that current numerical methods usually do not predict the temperature stratification in the core region of the cavity correctly [1]. In order to increase the realizability of the boundary conditions in experiments with air filled cavities, a linear temperature distribution is usually proposed instead of the adiabatic assumption [2]. Other experimental investigations provide benchmark data for the validation of numerical codes [3],[4].

The range of experimental data is mainly restricted to the laminar and low turbulent flow regimes. As in the majority of engineering flow problems turbulence is involved, it would be desirable to extend experimental data to cases with higher turbulence intensity. Because the solving of the Navier-Stokes equations with turbulent effects requires a very fine grid and small time steps, direct numerical simulations (DNS) are computationally too costly for engineering purposes. Instead, time averaging of the equations is usually employed, eliminating the need to solve the time dependency caused by turbulence. However, this approach yields additional unknowns that have to be estimated through a conveniently chosen turbulence model. The method to choose strongly depends on the problem at hand and new methods for broader application and better performance are continuously sought. Therefore there is a need for experimental data on turbulent flows for validation purposes, which are too scarce at the moment. Despite the geometric simplicity, differentially heated cavities provides challenging features for numerical modeling, because of the presence of turbulence and steep gradients near the walls and a nearly stagnant core region.

Accurate DNS calculations also prove to be good validation material and were performed on a cavity with aspect ratio four [5], similar to the geometry considered in this work. Different levels of turbulence are considered, using the parameter $Pr = 0.71$ to resemble the flow of air. In the present experimental research a matching degree of turbulence is aimed for using water, therefore complementing the data with results for $Pr = 7.0$.

2 Theory

Obviously the velocity and temperature distributions in a differentially heated enclosure can not be solved analytically. In such cases the analysis can be carried out by using either experiments or applying an appropriate numerical method. Several variables are involved and it is a common practice to reduce them to a few dimensionless numbers. With the use of the Buckingham Π theorem, the number of variables governing a specific problem can be narrowed down to just a few dimensionless numbers. In the case of natural convection the most important number is the Rayleigh number, describing the qualitative ratio between buoyancy forces and viscous forces:

$$Ra_H = \frac{g\beta\Delta TH^3}{\nu\alpha} \quad (2.1)$$

with α being the thermal diffusivity and β the thermal expansion coefficient of the fluid. In the case of the cavity considered herein, the temperature difference between the heated walls is used and the height H is recognized as the relevant length scale. The driving forces of the natural convection appear in the numerator of the Rayleigh number, so the higher the Rayleigh number, the stronger the natural convection. Geometrically similar problems will show transition from laminar to turbulent natural convection at the same Rayleigh number independent of the fluid used. The transition in a differentially heated cavity occurs around $Ra = 2 \cdot 10^8$, somewhat depending on the surface roughness. Furthermore the solution depends on the Prandtl number:

$$Pr = \frac{\mu c_p}{k} \quad (2.2)$$

The Prandtl number describes the ratio between the momentum diffusivity to the thermal diffusivity. As heat is the driving force for the momentum boundary layer, the Prandtl number has an important influence on natural convection, affecting the thickness of the momentum and thermal boundary layers. Most found Prandtl numbers in literature are those of water and air at atmospheric condition, being close to 7 and 0.7, respectively.

2.1 Governing equations

As the expected velocities in the solution are expected to be very low compared to the speed of sound in the fluid and the temperature difference between the vertical walls is small, a good starting point would be the incompressible Navier-Stokes equations. The PDE conservation forms of such governing equations are:

$$\frac{\partial \vec{u}}{\partial t} + \vec{u} \cdot \nabla \vec{u} = -\frac{1}{\rho} \nabla p + \nu \nabla^2 \vec{u} + \vec{g} \quad (2.3)$$

Provided that the gravitation vector is the only source of body forces. Incompressibility reduces the continuity equation to the following expression:

$$\nabla \cdot \vec{u} = 0 \quad (2.4)$$

Because the flow is driven by temperature differences, the energy equation needs to be considered too:

$$\rho \frac{\partial E}{\partial t} + \rho \nabla \cdot (\vec{u}H) = \rho \vec{u} \cdot \vec{f} + \nabla \cdot (\bar{\tau} \vec{u}) + \nabla \cdot (k \nabla T) + \dot{Q} \quad (2.5)$$

Note that despite incompressibility is assumed, the buoyancy forces are taken into account through a thermal expansion coefficient that gives rise to the body force \vec{f} . These five equations can be rewritten into a general form with the conserved variable ϕ that can be solved with commercial software, such as Fluent, applying the finite volume method [6].

$$\frac{\partial \phi}{\partial t} + \nabla \cdot (\phi \vec{u}) = \frac{1}{\rho} \nabla \cdot (\Gamma \nabla \phi) + \frac{1}{\rho} S_\phi \quad (2.6)$$

The left side of equation 2.6 represents the local increase of the variable in time and the convective outflow of the fluid element. This is forced to be equal to the increase of the variable by the diffusion and the volumetric source term on the right side.

2.2 Turbulence modeling

The governing equations could be solved directly without applying a model for turbulence. However, in order to capture the physics, an unsteady simulation with small time steps should be applied on a very fine grid, taking months on a simple problem in order to have enough data to perform statistics on the turbulence.

2.2.1 Time averaging

Usually one is not interested in the behavior of individual eddies in a turbulent flow, but rather wants to know the mean behavior and the occurring deviations because of these eddies. For this purpose the variables are decomposed into a time averaged part and the fluctuating part caused by the turbulence, before substitution in the governing equations. Lets consider the decomposed velocity vector $\vec{u} = \vec{U} + \vec{u}'$ and the decomposed pressure $p = P + p'$, substituted them into the momentum equations 2.3 and see what happens when the terms are averaged in time:

$$\overline{\frac{\partial(\vec{U} + \vec{u}')}{\partial t}} + \overline{(\vec{U} + \vec{u}') \cdot \nabla(\vec{U} + \vec{u}')} = -\overline{\frac{1}{\rho} \nabla(P + p')} + \overline{\nu \nabla^2(\vec{U} + \vec{u}')} + \vec{g} \quad (2.7)$$

By definition the averages of the fluctuating parts are zero when appearing in linear forms, simplifying the above expression to:

$$\frac{\partial \vec{U}}{\partial t} + \vec{U} \cdot \nabla \vec{U} + \overline{\vec{u}' \cdot \nabla \vec{u}'} = -\frac{1}{\rho} \nabla P + \nu \nabla^2 \vec{U} + \vec{g} \quad (2.8)$$

Bringing us back to the same momentum equations 2.3 but for the six introduced non-linear terms of the perturbations in the velocity field $\overline{\vec{u}' \cdot \nabla \vec{u}'}$, referred to

as the Reynolds stresses. Applying the same strategy to the energy equation 2.5 yields three similar terms representing correlations between temperature and velocity perturbations. Note that the continuity equation 2.4 does not change in this evaluation, the velocity components are just replaced by the time averaged velocities.

2.2.2 Closure problem

The new set of equations are called the Reynolds Averaged Navier-Stokes equations (RANS). The new terms, consisting of the fluctuations in the velocity components and temperature are unknown and pose the closure problem of the RANS equations.

Observations of turbulent flows showed that the largest values of the fluctuations in the velocity field are found in the regions where the mean velocity gradient is largest. This has led to the Boussinesq approximation, relating the Reynolds stresses to mean flow velocity gradients with a viscosity-like constant μ_t called the turbulent viscosity.

$$\tau_{ij} = -\overline{\rho u'_i u'_j} = \mu_t \left(\frac{\partial U_i}{\partial x_j} + \frac{\partial U_j}{\partial x_i} \right) \quad (2.9)$$

The analogous turbulent transport of the thermal energy takes the form

$$-\overline{\rho u'_i T'} = k_t \frac{\partial T}{\partial x_i} \quad (2.10)$$

Usually the assumption is made that the turbulent temperature diffusivity is equal to a fraction of the turbulent viscosity $\sigma_t k_t = \mu_t$, defined by the turbulent Prandtl number σ_t . The only thing left now is to find a proper expression for the turbulent viscosity and the closure problem is solved.

2.2.3 Mixing length

The first attempt to find an expression for the kinematic turbulent viscosity ν_t was by means of dimensional analysis. The dimensions $[m^2/s]$ were sought by the multiplication of physically relevant length and velocity scales, yielding

$$\mu_t = \rho \nu_t = \rho l_m^2 \left| \frac{\partial U}{\partial y} \right| \quad (2.11)$$

which proved pretty accurate for simple two-dimensional flows. The length scale is a combination of the physical relevant length and an experimentally obtained constant belonging to a certain problem. This method is called Prandtl's mixing length model.

2.2.4 $k - \varepsilon$ model

In an attempt to develop a model that is more generally applicable, the $k - \varepsilon$ model was developed. The model computes the turbulent viscosity from two

more variables that are solved in the domain. One equation for the turbulent kinetic energy $k = \frac{1}{2}|\bar{u}'|^2$ and another for the viscous turbulence dissipation are assembled to the best knowledge of the physical behavior. In these equations four adjustable constants are present that are set to a value such that a wide range of turbulent flows is solved accurately. A fifth constant is found in the equation of the turbulent viscosity from k and ε : $\mu_t = \rho C_\mu k^2/\varepsilon$. This is the simplest general model to close the RANS equations, supplying reasonable results for some engineering applications. The main drawback for this method and variations on it like the $k - \omega$ method, lies in the fact that it assumes the turbulent viscosity to be an isotropic scalar, which is not accurate for flows with for example complex strain fields or significant body forces.

2.2.5 Reynolds stress equation model (RSM)

The more complex turbulence model RSM solves transport equations for all six independent Reynolds stresses instead of just the kinetic energy. The turbulent dissipation ε needs to be resolved, yielding seven equations for the model required to solve the turbulent flow. This method is the most general of the classical turbulence models, but computational costs are considerably higher compared to $k - \varepsilon$. The major uncertainty comes from the modeling of the turbulent dissipation [6].

2.2.6 Large eddy simulation (LES)

LES can be considered as an efficient midway between the computational costly DNS and turbulence models based on the RANS approach. The large eddies, containing most of the turbulence kinetic energy, are resolved directly, while the more isotropic behaving, low-energy containing small eddies are modeled applying the Boussinesq approximation. The mesh resolution generally acts as the filter to separate these two scales and therefore determines the smallest eddy that will be resolved. On one hand computational cost is much higher than even RSM, but on the other hand it is way lower than for a full DNS simulation.

2.2.7 Wall treatment

When a turbulent flow is bounded by a wall, this will affect the turbulent quantities. The no-slip and impermeability conditions not only apply to the main flow, but also to the fluctuations. On the other hand the velocity gradient near the wall will act like a source of turbulence. Good near-wall modeling is therefore in general very important, while most turbulence models are developed to predict free-stream turbulent behavior [7].

A turbulent boundary layer can be subdivided into a viscous sublayer very near the wall where molecular diffusion plays a dominant role, fully-turbulent region further away from the wall, and a transition region between them. The solution can be solved up to the wall, but this requires a very fine mesh for the high gradients in the mean and turbulent quantities. At least some volumes

must lie within the viscous sublayer for accurate results. Another approach is to apply wall functions, semi-empirical functions describing the behavior of the turbulent quantities near the wall. This approach obviates the need of a very fine mesh to solve the boundary layer, which might drastically reduce computational time. However, special care has to be given to the validity of the wall functions for the type of flow being considered, which can include effects as strong adverse pressure gradients.

3 Numerical simulation

Numerical calculations were carried out on the differentially heated cavity configuration shown in figure 1. Validation data is found in the DNS data of [5], published in 2007. Their data consists of a fluid with $Pr = 0.71$, varying the Rayleigh number in five steps from $6.4 \cdot 10^8$ up to 11^{10} . For validation of the turbulence models the lowest Rayleigh $6.4 \cdot 10^8$ and the one that will be established in the experiments 10^{10} are taken for comparison.

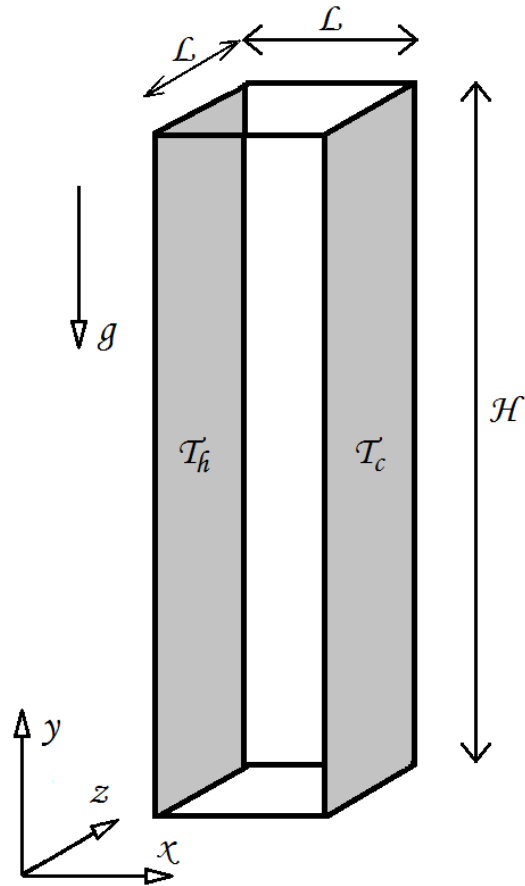


Figure 1: Schematic representation of the cavity

3.1 Solution procedure

The numerical models have been applied to the same conditions as the DNS data. All models applied are solved up to the wall, so wall functions are not

applied. First laminar calculations are performed by setting the gravitational constant a factor 100 lower. This solution is used as initial guess for the turbulence models. After convergence is reached, velocity, temperature and turbulent intensity values are read and compared along certain lines in the domain. The solutions have been verified for truncation error, by means of mesh-refinement tests. A grid size of 100x250x50 (x,y,z) proved to be sufficient. The calculations are all conducted by the commercial code Ansys Fluent 12.0.

3.2 SST $k - \omega$ model

The first and simplest model considered is the Shear-Stress Transport (SST) $k - \omega$ model. The model $k - \omega$ differs from the briefly described $k - \varepsilon$ model in that it resolves for the specific dissipation rate ω , rather than the turbulence dissipation rate ε which has proven to be more accurate for wall-bounded flows. The SST adopts the $k - \omega$ model near the wall and the $k - \varepsilon$ model further away from the walls, making the model more generally applicable compared to the standard $k - \omega$. The result of velocity and temperature profiles at 20, 50 and 80 percent of the height of the cavity is shown in figure 2 and 3.

3.3 RSM

The second model applied is the RSM model. The converged solution of the $k - \omega$ model served as the initial guess for this more advanced model. This model should be able to produce better results near the wall and in the corners where the streamline curvature is relatively high. These results are also included in figure 2 and 3.

3.4 Conclusions

At the lower turbulence intensity both models show pretty good agreement with the DNS data, the $k - \omega$ model seems to overestimate the momentum diffusion and RSM overestimates the maximum velocity. Both models slightly underestimate the temperature stratification over the cavity height. Also the results for the local Nusselt number along the heated walls are accurate for the lower Rayleigh number, see figure 4. At the higher Rayleigh number the deviations in the velocity between the models and the DNS are unacceptably high.

Of course the best variables for the validation of turbulence modeling are the turbulence quantities, like the turbulence intensity $I_t = \frac{k}{1/2|\bar{u}|^2}$. For the $k - \omega$ model the magnitude of the turbulence intensity is accurate, but the distribution is not, probably because the turbulence is modeled by two equations only. Although the solution of the RSM appears to be more accurate, strangely the turbulence intensity is found to be virtually zero in the hole domain. In fact, for an unknown reason, the model finds a laminar solution for the problem, explaining the over-prediction of the velocity because there is no additional viscous dissipation as a result of the turbulence.

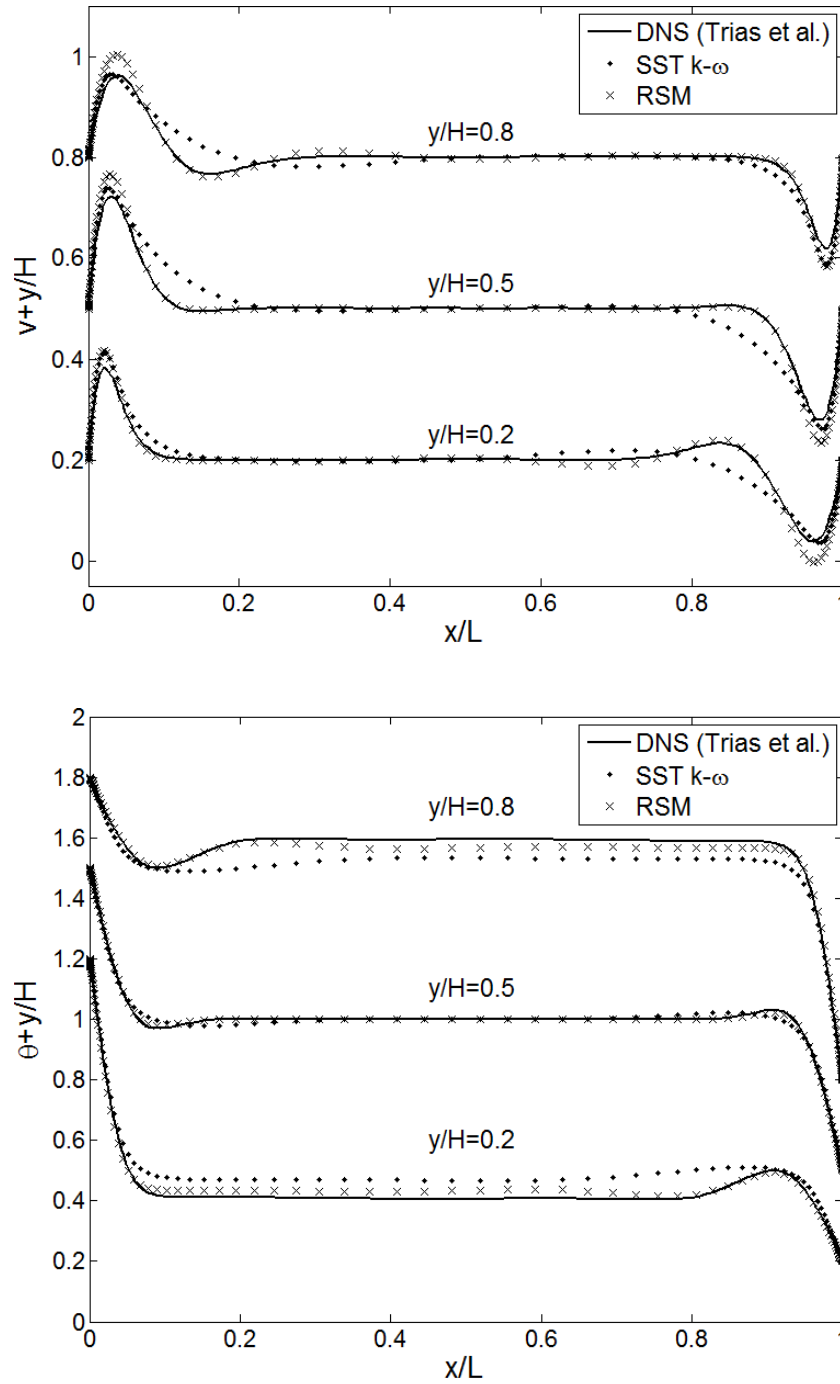


Figure 2: Comparison of velocity and temperature profile at $Ra_H = 6.4 \cdot 10^8$

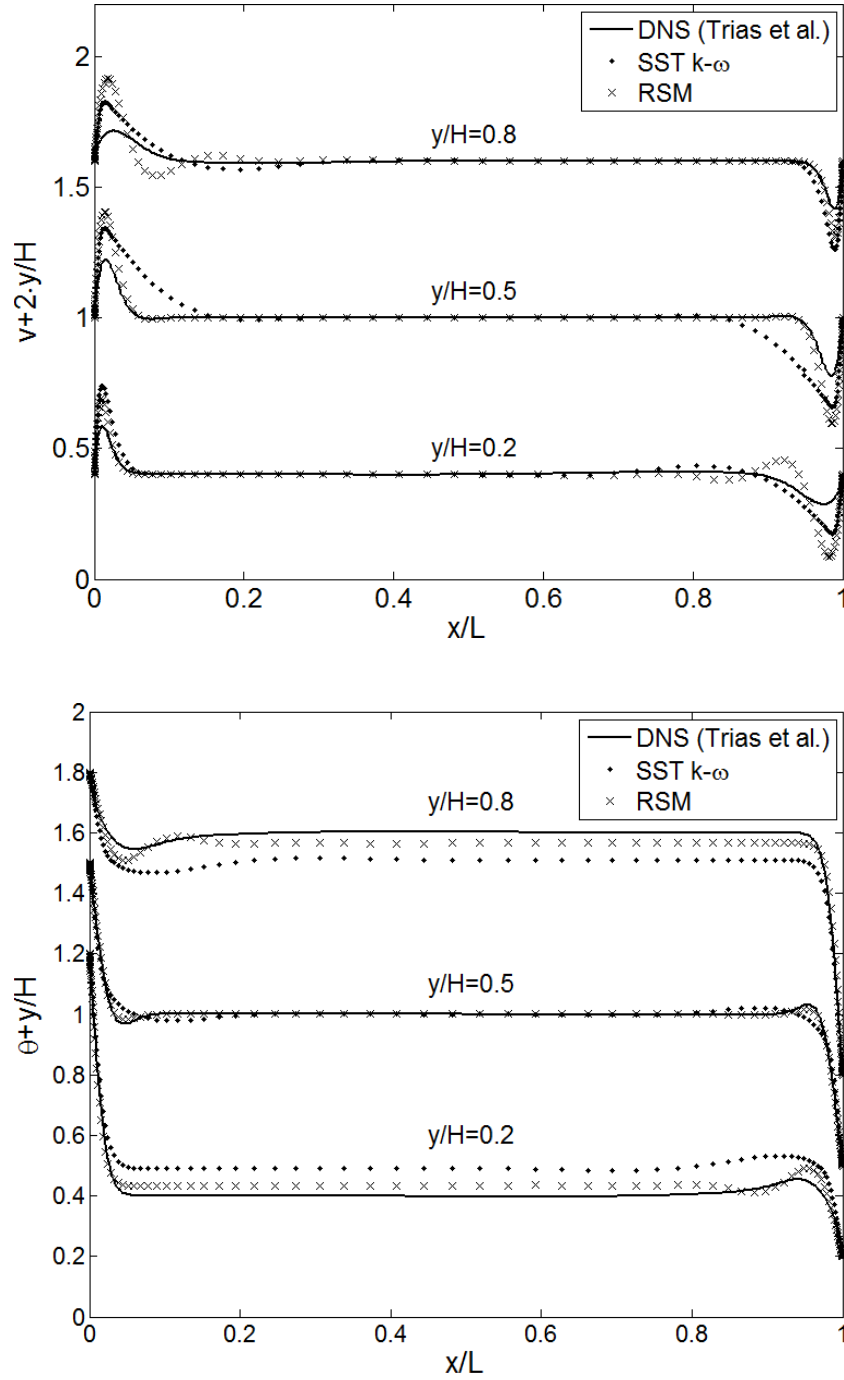


Figure 3: Comparison of velocity and temperature profile at $Ra_H = 10^{10}$

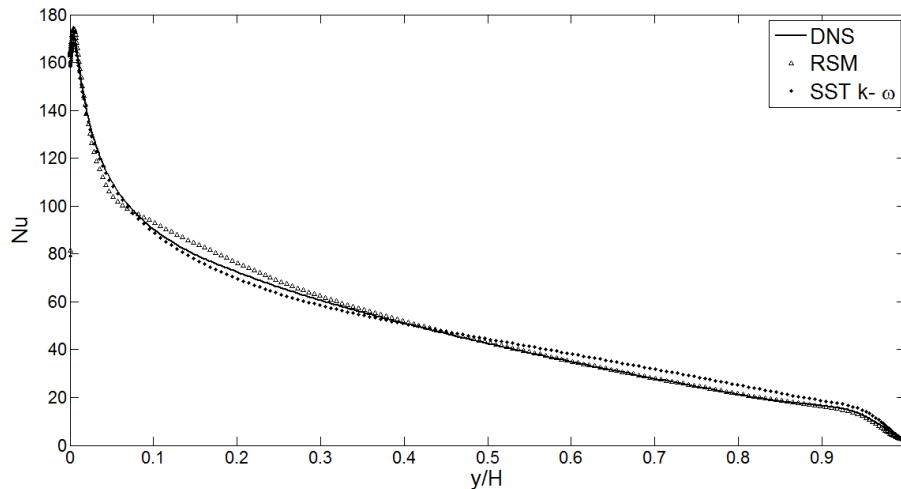


Figure 4: Local Nusselt number along the heated wall, $Ra_H = 6.4 \cdot 10^8$

3.5 Large eddy simulation

Since the RSM was found unable to capture the turbulence quantities in the solution, LES was also carried out in the present study. As the computational efforts are some magnitudes of order higher than the previous models that sought a steady state solution, the computational power of a cluster is exploited.

3.5.1 Mesh design

The mesh used for the LES model is developed with the use of the validation data. As the mesh size determines the size of the resolved eddies, it is important to use a fine and consistent grid in the region with high turbulence intensity. A mesh density function is chosen based on the turbulence kinetic energy. Figure 5 shows the turbulence kinetic energy at the lower Rayleigh number with the density function scaled to the same order of magnitude.

Near the wall a constant distribution is used and in the middle of the cavity the density is 20 times lower. A smooth transition is applied between those regions. The turbulent kinetic energy for the high Rayleigh number has similar magnitude, but is located closer to the wall. With this density function 150 points are distributed in the x-direction between the heated walls. In the other directions bi-exponential density functions are applied, yielding close to cubic volumes in the cavity core and a fine distribution near the walls, placing the first volume well within the viscous sublayer.

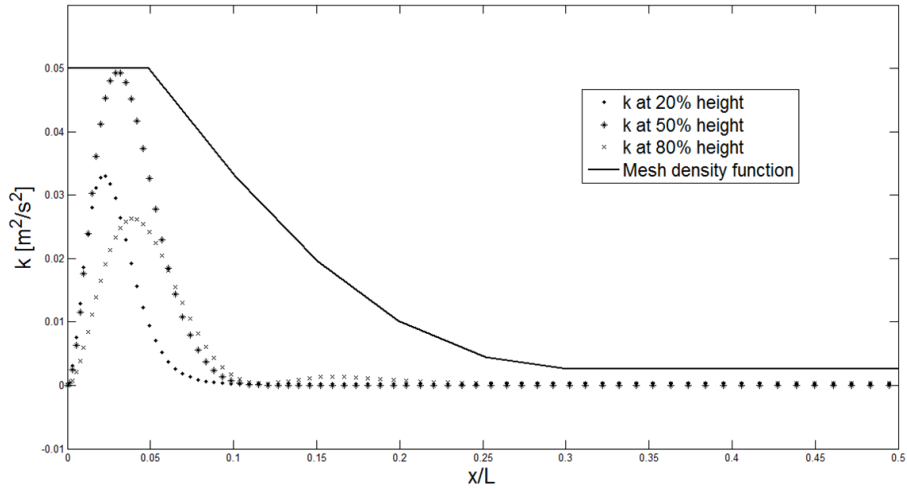


Figure 5: Turbulence kinetic energy and the density function for the LES-mesh

3.5.2 Journal file

The Fluent application running on the cluster is controlled by a sequence of commands listed in a so-called journal file. In order to export variable data for every time step and apply autosave, loops had to be written in Scheme programming language which is supported by Fluent. With the help of [8] a journal file could be written to retrieve the required data automatically.

Moreover Matlab codes were written to read the data for the calculation of the statistical variables and visualize physically relevant variables such as isocontours of temperature and Reynolds stresses. A screen-shot of a resulting movie of temperature profiles in the top quarter of the cavity is shown in figure 6.

3.5.3 Solution procedure

An attempt was made to solve the problem explicitly, being computationally cheap for solving with small time steps. Unfortunately the solution did not converge, even for very low Courant numbers. Instead the implicit scheme is used, roughly requiring a week to gather enough data for statistically stable solution on a cluster node with eight processors. Due to some problems with the cluster there are no statistically stable results yet to show.

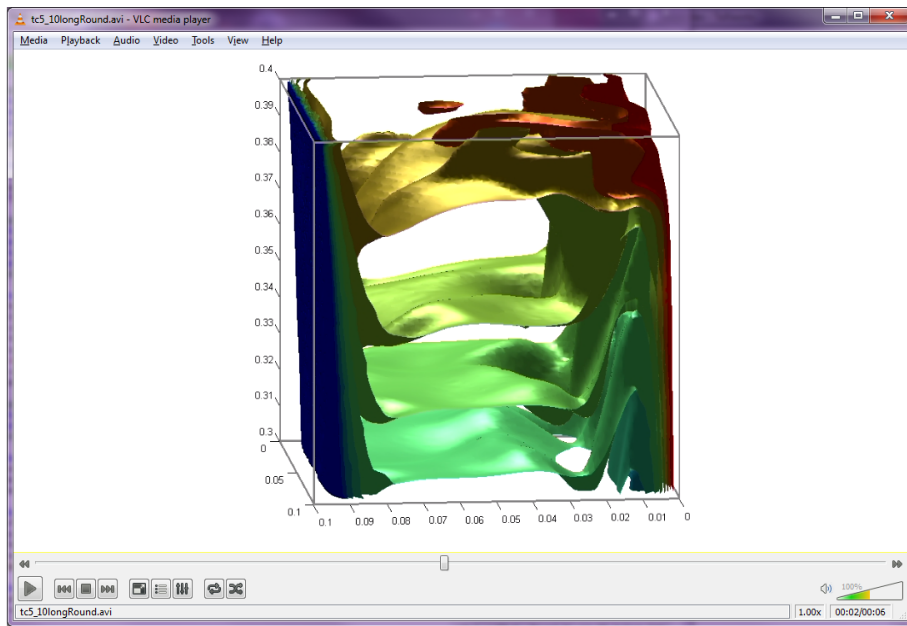


Figure 6: Temperature isocontours in the top of the cavity, LES $Ra_H = 6.4 \cdot 10^8$

4 Experimental setup

The cavity, shown in figure 1, has a square base and an aspect ratio of 4, giving it the dimensions 100x400x100 mm. The cavity is positioned vertically, aligning the longest side with the y -axis. As the gravitational force acts along the y -axis, the Rayleigh number is based on the height H . The temperature of the aluminum walls perpendicular to the x -axis can be controlled in order to apply the differential heating to the cavity. The front, back, top and bottom of the cavity are constructed from PMMA, enabling optical measurement techniques to retrieve data. The fluid to be studied in the cavity is water.

4.1 Cavity

This section describes the positioning of the cavity in the laboratory. The temperature management is considered and special attention is given to the thermal boundary conditions defining the problem and creating the possibility to compare the experimental results to future numerical calculations.

4.1.1 Environment

The ambient temperature inside the laboratory is kept constant at $20^{\circ}C$ by the air conditioning system, with an accuracy of $1^{\circ}C$. The cavity is placed on a suspended table, isolated from external vibrations (heavy traffic, working laboratory technicians etc.) by a set of springs. The setup is shielded by black curtains, primarily for the safety of the laboratory technicians, but it also prevents ambient light to influence the measurements.

4.1.2 Radiation

With water as the applied working fluid, the used dimensions guarantee a temperature difference of around $10^{\circ}C$ in order to reach the turbulent flow regime up to the aimed value of $Ra_H = 10^{10}$. Combined with the low emissivity of the aluminum heating walls, this assures that radiation will be negligible compared to the heat flux caused by the natural convection.

4.1.3 Thermal boundary conditions

Heated walls The desired boundary condition of the heated walls is a uniform temperature. This condition is approached by the high conductivity of the aluminum wall material, kept at temperature by a steady supply of water from a thermostatic bath meandering trough canals embedded in the walls. Measurements with thermocouples show a maximum deviation of $0.6^{\circ}C$ from the aimed isothermal temperature.

Remaining walls The non-heated walls are meant to behave adiabatically. The measurement techniques require the walls to be transparent, making good isolating properties hard to achieve. A high thermal resistance is established

by the use of one inch thick PMMA walls instead of the better heat conducting glass alternative. Moreover a low heat flux through the sidewalls is guaranteed by the small temperature difference of the flow with respect to the controlled ambient temperature.

4.2 Measurement instrumentation

For the LDV, PIV and LCT measurements, instrumentation is positioned around the cavity. In order to be able to capture the desired data, the instrumentation that has to be repositioned is mounted on a positioning table with three remote controlled translational degrees of freedom.

4.2.1 Positioning system

The positioning system used is the T3D Standard Traverse System of TSI, specially designed for applications such as LDV and PIV measurements. The system is remote controlled by computer and is integrated with the measurement control of the LDV and PIV systems. The three axis can be positioned over a range of $600mm$ with an accuracy of $300\mu m$ and a repeatability of $10\mu m$. The profiles which are part of the table assures flexible use and a rigid fixture of the instruments.

4.2.2 LDV

The Laser Doppler Velocimetry instrumentation consists of a laser with a multicolor beam separator and a transmitting probe with integrated receiver. The probe is connected to the beam separator with a flexible cable and can therefore be positioned freely by the table to measure the points of interest within the cavity. The same probe collects the data by the backscatter of the seeding particles passing the focal point. Particles reflect the laser light with a certain frequency caused by crossing a fringe pattern, hence the velocity can be calculated. The data is processed by the Photo Detector Module and Signal Processor before it can be accessed on the computer with FlowSizer software.

4.2.3 PIV

For the Particle Image Velocimetry another laser, emitting a white light, is fixed to the positioning table. The laser illuminates a cross-sectional plane in the cavity from above. A static camera captures the illuminated seeding particles (larger than the particles used for LDV) in a frequency so that the velocity can be constructed with by correlation between the particles in the images. The wanted data can be obtained by PowerView software.

4.2.4 LCT

The Liquid Crystal Thermography technique uses encapsulated crystal seeding particles that change color according to the temperature in a certain range. A

sheet of white light from a bright lamp above the cavity defines the plane of interest, as in the PIV experiment. A 3CCD camera captures the color field, that - after proper calibration - can be converted numerically to a temperature field.

4.2.5 Wall heat flux measurement

For the measurement of the wall heat flux at the heated walls of the cavity, walls with integrated heat flux sensors are installed. These walls are not used in the other experiments, because the use of these sensors might introduce an additional error in the uniform temperature of the heated walls that can unnecessarily compromise the accuracy of the other measurement techniques. A wall contains eight sensors distributed over the height, making it possible to calculate the Nusselt number along the wall.

5 Laser Doppler Velocimetry

LDV is the first experiment to be carried out. The setup was used before in the laboratory and all components were still in place and connected. The settings though had to be re-optimized and optical components had to be checked and cleaned. The details of the used instruments for LDV is listed in Appendix A.

5.1 The optic system

The heart of the setup is an argon ion laser, emitting a beam consisting of specific wavelengths. Because of the high power requirement of such a laser, it is equipped with water cooling. Approximately ten liters of filtered water per minute is used to remove excess heat. A beam splitter extracts two wavelengths from the laser beam that will be used to measure the two velocity components. A Bragg cell divides these wavelengths in two, with a shift in frequency between the pairs. The two pairs of laser light leaving the beam splitter are led into individual optic fibers by couplers. The fibers transport the beams to the probe that is dynamically positioned on the traverse system in front of the cavity.

After the beam splitter was properly aligned with the laser, the couplers had to be adjusted so the light is focused precisely at the entrance of the fiberglass. Thereto a focusing ring and a course and a fine set of positioning knobs are available on the couplers to steer the green (514.5 nm) and blue (488 nm) light that is used. A laser power meter is put in front of the probe allowing to maximize the efficiency of every coupler. The argon ion laser itself is adjusted to optimize the combined intensity of the beams. The power of both wavelengths are found to be of the same order of magnitude.

For proper functioning of the LDV, the pairs of beam paths have to cross exactly at the focal point. Here fringes will develop because of interference between the paired beams. The misalignment of beams in the crossing point is found to fall within the specifications. The frequency shift induced by the Bragg cell in the beam splitter causes the fringes to travel with a constant velocity within the oval focus point.

Another important feature of the beams is the polarity of the light. In order to obtain a sharp contrast between the fringes, the polarity of the pairing beams need to be similar. The polarization angle of a beam is found with a Polarization Axis Finder, the angles were assessed to be very accurate. The amount of polarization is not very high, but believed to be sufficient, this property is found by the contrast of the image created with the Polarization Axis Finder.

The fact the measurements are carried out through a window and in another medium give extra complications. Refraction and reflection of the laser beams have to be considered for valid measurement results. Luckily the the solutions are straightforward in the case the probe is placed perpendicular with respect to a flat window, and also applicable for small offset angles. Reflections from the PMMA walls will fall exactly on the same line as from where they were sent. In order to prevent these reflections to influence the measurements from particles passing through the focal point, a mask is made that is placed in front

of the probe, masking the horizontal and vertical lines between the emitted beams. The focal point itself is not influenced by the media because of the perpendicularity, only the focal length changes with the distance to the window [9]:

$$F = F_D \frac{\tan \kappa_a}{\tan \kappa_f} + t \left[1 - \frac{\tan \kappa_w}{\tan \kappa_f} \right] + d_1 \left[1 - \frac{\tan \kappa_a}{\tan \kappa_f} \right] \quad (5.1)$$

In this expression the new focal length is expressed in the lens's focal distance, the wall thickness and the probe's distance to the window. The variable κ is the half angle between the beams in the air, window and fluid respectively. We are interested in the displacement of the focal point with respect to a displacement of the probe. Thereto we differentiate the expression with respect to the distance to the window: $\frac{dF}{dd_1} = 1 - \frac{\tan \kappa_a}{\tan \kappa_f}$. The angle of the beams in the fluid is found with Snell's law $\kappa_f = \sin^{-1}(\sin \kappa_a \cdot N_a/N_f)$, as a function of the refractive indexes. Recognizing that the displacement of the focal point is the displacement of the probe plus the change of focal distance yields:

$$\frac{dx_F}{dx_P} = \sqrt{\left(\frac{N_f}{N_a \cos \kappa_a} \right)^2 - \tan^2 \kappa_a} = 1.33 \quad (5.2)$$

So put in words, the focus point travels one third faster than the probe in the z-direction. This result will be used for positioning the focal point to the desired depth in the cavity.

5.2 Test measurements

To get acquainted to the measurement technique and find the optimal conditions, some test measurements are carried out on a prototype cavity. The quantity that will be measured is the frequency content of the backscattered light. When a particle crosses the focal point of the laser beams this causes an increased intensity. The frequency of the passing of a particle will be up to about the kHz range, depending on its velocity. A higher frequency will be super-positioned on this signal because of the moving fringes within the focal point. This signal will be in the MHz range; the 40 MHz of the shift applied by the Bragg cell plus the Doppler effect as a result of the particle velocity perpendicular to the fringes. Above this order of magnitude in the frequency the noise will prevail.

For seeding, polyamide particles are suspended in the flow with an average diameter of $5\mu m$. The particles have a density very close to the density of water, making them follow the flow accurately. Because of the low velocities in the experiment the passing frequency of the particles through the focal point is also low. This cannot be overcome by increasing the amount of particles, when too much particles are used the water is saturated and the seeding particles settle at the top wall. Also larger particles are available, but they will span several fringes, reducing the quality of the signal. In order to obtain a higher data rate it is attempted to measure while moving the probe along the line of measurements, hoping more particles would cross the focal point. Unfortunately the

data rate did not increase while it did bring other complications, therefore this strategy was rejected.

The signal processing equipment will first filter out the particle passing frequency with a high pass filter of 20 MHz. Subsequently the signal frequency can be 'downmixed', the subtraction of a fraction or the entire 40 MHz shift. This allows the Doppler frequencies, containing the velocity information, to fall in a certain Band Pass Filter range. The smaller the range can be chosen, the better the resolution of the resolved velocity will be. The maximum velocity to be expected is about 7 mm/s and the fringe spacing for the used blue light is $3.73 \mu m$. The maximum Doppler frequency will therefore be about 2 kHz. This assures that the boundary layer at one side of the cavity can be fitted exactly within the smallest frequency range available, when leaving a 1 kHz shift with the downmixing.

The most interesting region of the flow is of course the boundary layer, very near the wall. The measurement technique though uses an angle for the crossing beams. So to measure the horizontal velocity up to the wall an angle of at least 4 degrees is required, directing the focusing point to the wall. This implies that the entire profile, from wall to wall cannot be measured in one run, because the probe needs to be turned say ten degrees to capture both walls. Therefore it will be more convenient to measure both sides from the wall to the middle and connect both profiles with post-processing. Because of the angle the measured velocity is a combination of the z- and x-direction. As the z-velocities in the cavity are expected to be small compared to the other components and the used angle will be small, the contribution of the z-component will be neglected. A small investigation is carried out for the dependency of the results on the offset angle about the y-axis. Results of measuring perpendicular and with a 10° angle are compared. The results in figure 7 show that the influence of the measured z-component is very limited, but does indeed increase the measuring domain of the horizontal component considerably towards the wall. The unknown length of the gap from the last measurement to the wall that will still be present, is determined by drawing a third order polynomial through the measured vertical velocity in the boundary layer.

5.2.1 half-height, low turbulence

A test measurement is done at $Ra_H = 10^{10}$ near the hot wall in the middle of the cavity for the z- and y-axis. The probe is placed under an angle of 5 degrees to measure up to the wall. In figure 8 the obtained data of the vertical velocity component is compared to a *SST* $k - \omega$ numerical solution. As the numerical turbulence quantities converged to a questionable distribution, it only serves for qualitative comparison. Every experimental data point is the velocity average of about one hundred particles, taking more than a minute per measurement, so information about the turbulence will be captured in the statistics. The error zone shown is the standard deviation on both sides of the mean value. The deviations are relatively small and from the same order of magnitude of the

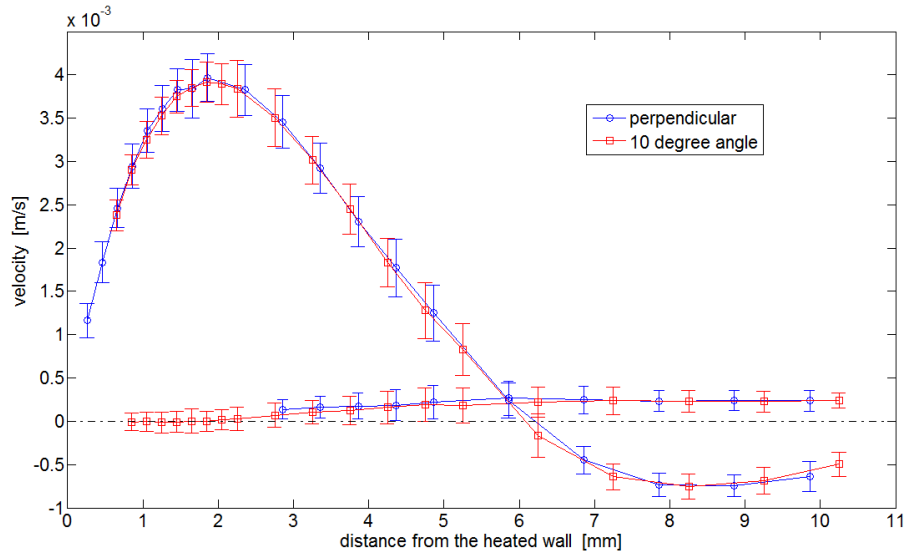


Figure 7: Influence of an angle about the y-axis on the measurements

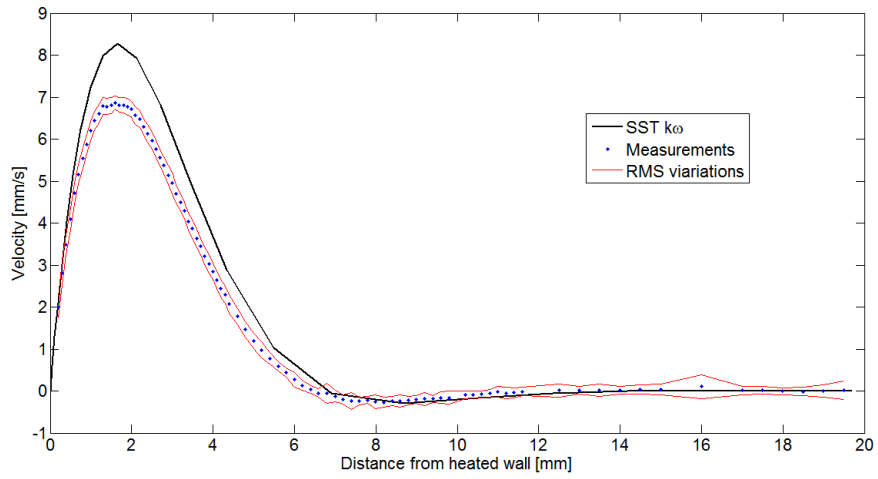


Figure 8: Laser Doppler Velocimetry measurements

measurement deviations of the stagnant fluid without heated sidewalls. Therefore with the low turbulence intensity at this height it is difficult to obtain information about the turbulence.

5.2.2 80 percent height, high turbulence

On 80 percent height of the cavity the turbulence kinetic energy is significantly higher, allowing to study the turbulence quantities more easily. At the point (5,320,50) in the boundary layer of the heated wall, 6 minutes of measurement yielded about 1700 velocity measurements per direction. This data clearly shows a fluctuating behavior due to turbulence. A statistical property of a signal is the autocorrelation function, correlating the signal with itself after applying a shift in time as defined in equation 5.3.

$$\rho(\tau) = \frac{\overline{u(t) \cdot u(t + \tau)}}{\overline{u(t)^2}} \quad (5.3)$$

This correlation is shown for the vertical velocity in figure 9. Obviously the correlation gives unity for zero time shift and lower in the rest of the domain. The correlation is decreased to zero after two seconds, before experiencing a significant overshoot. After about five seconds there is a positive peak again. A random signal would not have this oscillating behavior, but would rather converge to zero rapidly. The oscillation is a result of a dominant frequency of

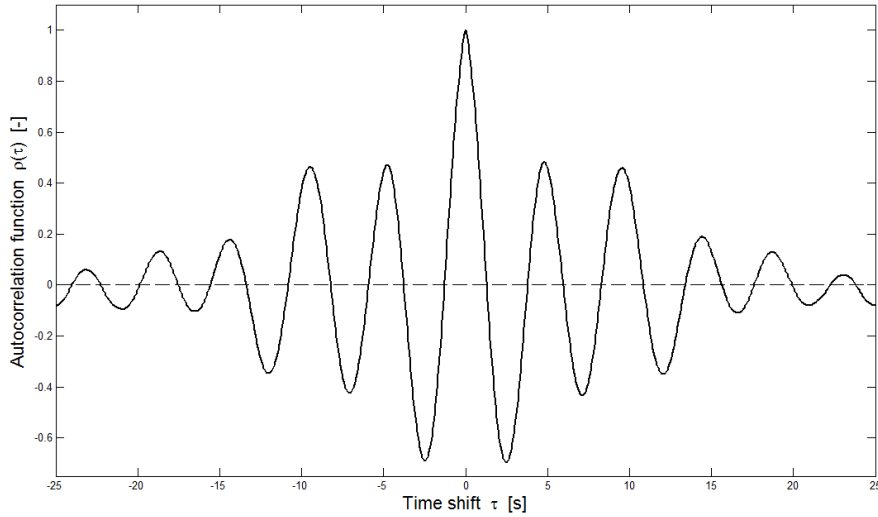


Figure 9: Autocorrelation function in a region of the cavity

passing eddies, which is about 0.22Hz as can be seen from the positive correlation after every multiple of 4.6 seconds shift. This obtained information on

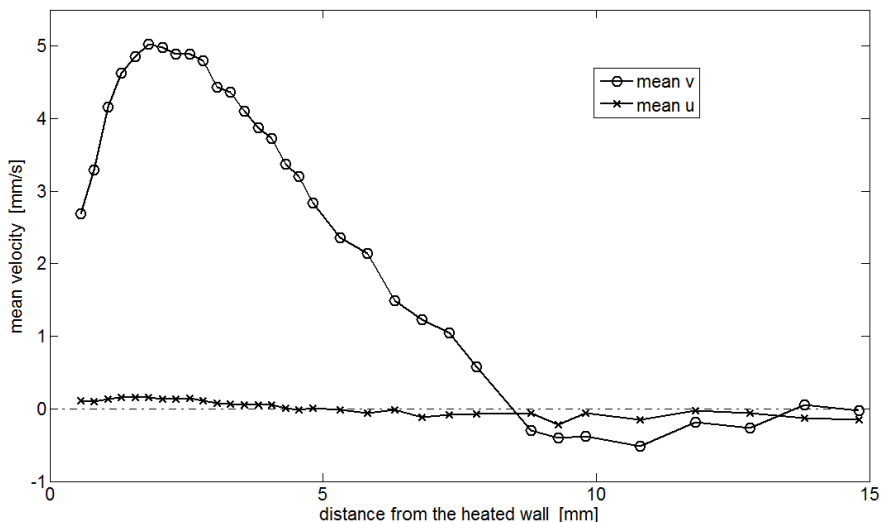


Figure 10: Mean velocity profiles at 80% height

the passing frequency of the eddies is important for the time to measure at a specific point in order to obtain statistically stable data. If measurements span about 100 eddies, a single eddy will have negligible influence on the statistics. This suggests that collecting 8 minutes of data at every position would give statistically stable quantities.

With 500 seconds per point, the boundary layer at 80% height is measured with the same settings as was done at 50% of the height. Velocities are only used if within a time window of 0.1s a measurement is done on both channels, giving the possibility to correlate the velocity deviations between the two directions in order to find the Reynolds stress. By mistake, the measurements are performed 7mm from the middle in the z-direction. In figure 11 the turbulence quantities for the two directions are visualized. Although sufficient particles are captured in the specified time, it does not give a really smooth result. The quantitative behavior and order of magnitude though are clear. The correlation of the velocity fluctuations between the two directions is low, but it is slightly negative very near the wall and positive further away from the wall, which seems to make sense, imagining growing eddies. The turbulence kinetic energy, defined by equation 5.4 is calculated assuming that w' is the mean of u' and v' , which is found to be the global behavior near the wall in the DNS data of the air-filled cavity.

$$k = \frac{1}{2} \left[\overline{u'^2} + \overline{v'^2} + \overline{w'^2} \right] \quad (5.4)$$

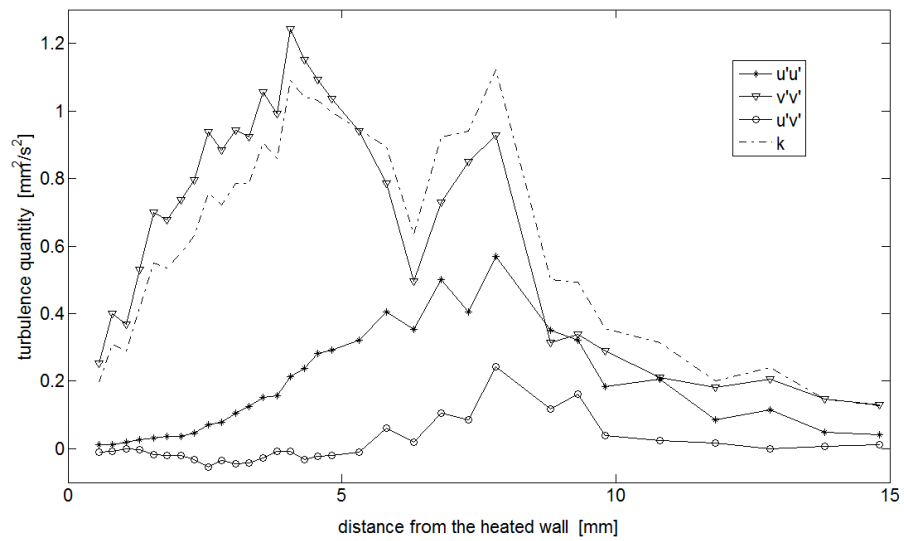


Figure 11: Turbulence quantities at 80% height

6 Particle Imaging Velocimetry

PIV was carried out more often in the past at POLO. The equipment was available and could pretty much be considered as plug and play. The main focus of this part was how to position the camera and laser with respect to the cavity. A special part was designed to attach the laser to the traverse system, so different plane depths can be illuminated with remote controlled traverse. The camera will be positioned on a stationary fixture. No further activities were carried out on PIV during the considered period.

7 Liquid Crystal Thermography

Liquid Crystal Thermography is a technique that allows one to measure the instantaneous temperature distribution in a plane, without disturbing the flow. The setup comprises a carefully selected illumination source, liquid crystal particles that are active in the right range and a sensitive color camera. The combination should guarantee clear images with a distinctive color to temperature relation. In this chapter the subsequent image processing, conversion to temperatures and the calibration method are considered.

7.1 Camera procurement

In this research the camera, capturing the color distribution from the illuminated plane in the cavity, plays a key role in the accuracy of the measurements. In LCT experiments usually CCD (charge-coupled device) cameras are used because of their excellent photosensitivity. As a CCD-chip in principle only registers intensity, optics have to be applied in order to extract information about the color contents. One option is to place a color filter on every single pixel, transmitting only red, green and blue alternately. This way two third of the incoming light is rejected and numerical interpolation has to be applied to reconstruct the color information in an RGB array. A more sophisticated method is to split the incoming light in three parts separated by specific wavelengths. The three components are directed to separate CCD chips, giving the name 3CCD to this technology. All incoming light is used and can be projected on RGB format directly, giving a very high resolution. Cameras with one CCD chip are considerably cheaper than its three chips alternative. With a certain budget roughly the same color resolution can be obtained. However, the single CCD camera needs an images of at least three times the size with the interpolated values that do not supply additional information. This increased image size is a disadvantage in post-processing time. These considerations have led to the decision to purchase a professional 3CCD camera for this research.

7.2 Image filtering

The images obtained with the 3CCD camera have to be processed before they can be used to calculate the temperature distribution. The images will be somewhat granular, because of the non-uniform crystal particle distribution. There will be voids, small regions without an illuminated particle, depending on the seeding density. As these dark spots contain no useful information, the color distribution has to be smoothed before the conversion to temperature. The main purpose of the image processing is to remove high differences in the color components of neighboring pixels. There are different approaches to filter out high frequency noise. The filtering process is a balance between noise reduction and preservation of the underlying physical behavior.

For the application of LCT image processing, combinations of linear filters have been applied. For example [10] subsequently applies a Fourier filter, and

averaging of a 5x5 window to reduce localized noise further. In order to get back some lost sharpness a high boost image preparation is applied. On the other hand non-linear filters are used for the processing of LCT images [11] with encouraging results. A median filter is applied to a 5x5 window to drastically reduce the noise content. A median filter returns the value that divides the high and low values in a window. This method is used to avoid corrupt data points to influence the other points. Because the voids are dark spots, containing no information about the flow, this would be a good strategy. Moreover the median filter manages to preserve edges and high gradients. The computational effort is somewhat higher, as the values need to be ordered before a value is assigned.

As separate filtering of the color components can give new color combinations, advanced median techniques for color images are considered [12]. The most straightforward method is the classic vector median filter, using either the L1 or L2 norm. The method is very costly in computation time and the gain in accuracy will be small compared to the median filter applied on the colors separately. This is because of the smooth nature of the problem, as no independent sudden color changes are expected and therefore no unrealistic new colors will be generated.

The three options above have been applied to an artificial LCT image sample, taken from [13], on a 5x5 filter window, with satisfactory result, see figure 12. What scheme to apply and with what window size will be chosen during calibration, when the amount of pixels in the domain and the size of occurring voids are known. The details of the filters that will be tested are listed below:

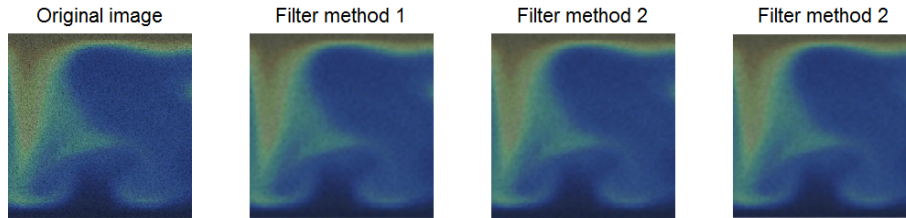


Figure 12: LCT image filtering on a sample

1. A 5x5 Gaussian Fourier filter with the parameter $\sigma = 1$ for optimal suppression of high frequencies, created in Matlab by the following command: `h=fspecial('gaussian',5,1)`. After this filter, the averaging of a 5x5 window is performed by `h=fspecial('average',5)`. Finally the sharpening process is carried out with the filter weights $\frac{1}{3} \cdot \begin{bmatrix} -1 & -1 & -1 \\ -1 & 11 & -1 \\ -1 & -1 & -1 \end{bmatrix}$, called up by the command `h=fspecial('unsharp',0.5)`. These schemes are applied with the Matlab function: `imfilter(image,h,'symmetric')`,

where special care is taken with the boundaries by the last entry. 'symmetric' mirrors the pixel values in the boundary, so no corrupt data enters the domain.

2. A median filter applied on a 5x5 window for the color components separately. The command `medfilt2(image(:,:,i),[5 5],'symmetric')` with the index denoting the color component.
3. A vector median filter applied on a 5x5 window: For every point in the window the absolute distance in the color space to the other points is calculated and added up. The middle pixel gets the lowest value of these L1 norms within the window. The code had to be written manually as Matlab only has a scalar median filter. The computation time is a few minutes, so for real time processing this filter is not suitable.
4. Identical to 1, with the Gaussian and averaging filters working upon a 7x7 window.
5. Identical to 2 applied to a 7x7 window.
6. Identical to 3, but on a 7x7 window.

7.3 Conversion to temperature

Once the images of the liquid crystals are smooth, an attempt can be made to transfer it to an accurate temperature distribution. As pointed out in [14] the correlation between the color and temperature can be carried out with one parameter for the color. But by the use of more parameters to describe the color, the accuracy and useful range of the spectrum might be increased.

7.3.1 One-parameter correlation

The color of the liquid crystal changes with the temperature, therefore the most convenient conversion to find the temperature corresponding to a certain color is to convert the RGB color components to the HSI space and find a correlation between hue and temperature. The conversion from RGB to the hue value is carried out with [15]:

$$H = \begin{cases} \cos^{-1} \left(\frac{\frac{1}{2}[(R-G)+(R-B)]}{[(R-G)^2+(R-B)(G-B)]^{1/2}} \right) & \text{for } B \leq G \\ 2\pi - \cos^{-1} \left(\frac{\frac{1}{2}[(R-G)+(R-B)]}{[(R-G)^2+(R-B)(G-B)]^{1/2}} \right) & \text{for } B > G \end{cases} \quad (7.1)$$

By curve fitting a one-to-one relationship between color and temperature is obtained.

The correlation between hue and temperature is usually not a simple monotonically increasing function. The useful range may therefore be restricted to the region where the hue is changing enough with temperature. When the slope becomes too small the error increases to unacceptable values. A reduction in

the error and an extension of the useful range might be obtained by combining the hue-temperature relationship with the dependency of temperature on saturation and/or intensity.

$$S = 1 - \frac{\min(R, G, B)}{\frac{1}{3}(R + B + G)} \quad (7.2)$$

$$I = \frac{1}{3}(R + B + G) \quad (7.3)$$

For a specific type of crystal liquids, a more monotonically increasing relationship is obtained by correlating the temperature to the hue divided by the intensity [14]. This method requires a combination of the variables that define a color in order to obtain the best correlation with the temperature, which will depend on the setup configuration and the characteristics of the used liquid crystal particles.

7.3.2 Neural networks

In the above strategy the three color components of an image are reduced to one parameter before a one-to-one conversion to the temperature field. Although pretty accurate results can be obtained by choosing the right parameter, better results can be obtained when no information is thrown away. By using all three color parameters in either RGB or HSI space, the error is reduced further and the useful range is maximized. The relation between the three variable color input and the temperature output can be obtained by means of an artificial neural network.

The neural network consists of one or more hidden layers between the input and output variables. By training the network with input data accompanied with the desired output, connections between neurons in the hidden layer will be assigned weights. After enough training the established network can convert the color images with high accuracy, given that the training data was a consequent set of data. In literature neural networks with four input parameters are also used. Besides the RGB values, also the corresponding hue is used as well [16]. As the hue is not independent of RGB, no additional information is provided to the neural network, but it can be seen as an extra weight on this most monotonically increasing parameter.

7.4 Calibration

The calibration has to provide the relationship between the color images and the temperature field. An inaccurate calibration will cause all obtained temperature fields to be erroneous, therefore this process has to be fulfilled with care. An important requirement for calibration is that the circumstances are the same as during the actual measurements. Although for example calibration with a dry substrate on a temperature controlled plate might be more accurate, it will not take into account effects because of dispersion in the fluid and voids between

particles which can be expected in the real measurement. For calibration of our setup there are two viable options for calibration.

1. Instead of applying differential heating, the temperature controlled walls are kept at the same temperature. When the temperature of the fluid is constant, the color is captured at the depth of the illuminating plane. This procedure is repeated for every tenth of a degree over the active range of the liquid crystals. The depths of the illuminated plane should be chosen the same as for the measurements as this will influence mainly the intensity of the received colors. This method will take some time as for every temperature step it will take time to reach a uniform temperature. Moreover it will yield a limited amount of data points with considerable uncertainty. A spline can be fitted through the filtered and averaged data for the one-parameter correlation. For the neural network a two dimensional filtered color field will give plenty of training data.
2. A second method relies on the physics of heat transport. When a stagnant fluid is subjected to a temperature difference, a constant heat flux and a linear temperature profile will develop. This situation can be obtained in the cavity if the present body force is eliminated. This is done by tilting of the cavity, such that the heated wall is on top and the cooled wall the bottom. Buoyancy will play no role in this configuration and a stratified temperature distribution will be found. Just one image can provide sufficient information for calibration. Most of the uncertainty will be in the temperatures at the walls, a smooth linear temperature distribution is assumed between these values. A filtered calibration image can be averaged over the x-axis, directly yielding a discrete correlation. For the neural network the horizontal lines are training data for one temperature. This method is the convenient choice and will be used if an accurate and reproducible correlation between color and temperature can be obtained.

8 Heat Flux

The experiments for obtaining the heat flux at the wall will be the last part of the research. Only for this last setup the heated walls will be equipped with heat flux sensors. The sensors are basically a small plate with known thickness and thermal conductivity with thermocouples measuring the temperature difference at both sides. This data can be converted to heat flux values straightforwardly. During the internship this particular part was not yet considered, only the design and positioning of the heat flux sensors was discussed briefly.

9 Conclusions

During the internship period some experience has been gained on numerically solving a buoyancy driven flow field, with turbulence involved. It is found that despite the developments in the field of computational fluid dynamics, obtaining a satisfying solution is not at all guaranteed. The combination of turbulent natural convection close to the wall and a stagnant core region with stratified temperature distribution proves to be a very challenging problem to solve numerically. Meshing and the solution strategy have to be adapted to the used model and chosen with care. When the calculation converges to a solution, the results have to be checked carefully for reasonable behavior.

The difficulties described above call for improved numerical models, especially for turbulent flows. This emphasizes the need for an extensive range of experimental data for validation purposes. The experimental data that will be obtained on the differential heated cavity will extend the available data to a region with higher turbulence intensity.

Preliminary results with LDV measurements show consistent and accurate results. The velocity profile can be measured up to a quarter of a millimeter close to the wall. In the region with higher turbulence kinetic energy, the separate eddies can be recognized and the behavior of Reynolds stresses can be determined.

PIV and LCT yet have to prove their accuracy and ability in extracting turbulent quantities. If the cameras are capable of capturing sharp images of the particles suspended in the flow at a sufficiently high rate, such data could be extracted. It should be noted that no statistics will be obtained on the correlation between temperature and velocity fluctuations, because the techniques will be applied separately. However, the effect of the turbulence quantities on the mean quantities will be captured in this research. Increased transport of heat and dissipation of momentum will be noticed and will be useful for validation purposes.

9.1 Postscript

This internship period has been a valuable experience. A good insight of the activities involved in experimental research is obtained, varying from a thorough understanding of the theory and using high end equipment, to solving practical problems and cleaning the test section. A lot has been learned on turbulence behavior and modeling on which I had no prior knowledge. Together with the abroad experience, this has been an internship I'll never forget.

I would like to thank Cesar Deschamps and Harry Hoeijmakers for making this internship possible, especially on such a short notice. Furthermore I would like to thank André Popinhak for his guidance and an enjoyable time in the laboratory.

10 Appendix A

Used instrumentation for particle doppler velocimetry:

Instrument	Description	Model
Laser	Water cooled Argon Ion Laser	Coherence Innova 70c 2
Multicolor beam separator	Splits beam and applies phase shift	fbl-2 Fiberlight
Fiberoptic Probe	Emits beams and collects backscatter	TR60 TLN06-363
Photodetector box	Converts light to electrical signal	PDM 1000
Signal processor	Processes the signal from the PDM	FSA 4000
Laser Power meter	Meter for laser power optimization	Coherent FieldMate
Seeding particles	Reflect light with a Doppler shift	Dantec PSP5

References

- [1] J. Salat, S. Xin, P. Joubert, A. Sergent, F. Penot, and P. Le Quéré. Experimental and numerical investigation of turbulent natural convection in a large air-filled cavity. *Int. J. of Heat and Fluid Flow*, 25:824–832, Apr 2004.
- [2] W.H. Leong, K.G.T. Hollands, and A.P. Brunger. On a physically-realizable benchmark problem in internal natural convection. *Int. J. of Heat and Fluid Flow*, 41:3817–3828, Feb 1998.
- [3] M.A.H. Mamun, W.H. Leong, K.G.T. Holland, and D.A. Johnston. Cubical-cavity natural-convection benchmark experiments: an extension. *Int. J. of Heat and Fluid Flow*, 46:3655–3660, Mar 2003.
- [4] Y.S. Tian and T.G. Karayiannis. Low turbulence natural convection in an air filled square cavity. *Int. J. of Heat and Fluid Flow*, 43:849–884, Jun 1999.
- [5] F. X. Trias, M. Soria, A. Olivia, and C.D. Pérez-Segarra. Direct numerical simulations of two- and three-dimensional turbulent natural convection flows in a differentially heated cavity of aspect ratio 4. *J. Fluid Mech.*, 586:259–293, Apr 2007.
- [6] H.K. Versteeg and W. Malalasekera. *An introduction to computational fluid dynamics*. Longman scientific & technical, first edition, 1995.
- [7] Ansys, inc. *Ansys Fluent 12.0 Theory Guide*, 12 edition, jan 2009.
- [8] Mirko Javurek. Scheme-programmierung in fluent 5&6. *unknown*, Oct 2004.
- [9] *TR/TM Series Fiberoptic Probes Owner’s Manual*, revision b edition, Nov 2005.
- [10] P.M. Lutjen, D. Mishra, and V. Prasad. Three-dimensional visualization and measurement of temperature field using liquid crystal scanning thermography. *J. of Heat Transfer*, 123:1006–1014, Oct 2001.
- [11] Yu Rao and Shusheng Zang. Calibrations and the measurement uncertainty of wide-band liquid crystal thermography. *Measurement Science and Technology*, 21:015105–015112, Nov 2009.
- [12] Andreas Koschan and Mongi Abidi. A comparison of median filter techniques for noise removal in color images. *Proc. 7th German workshop on color image processing*, 34:69–79, Oct 2001.
- [13] N. Fujisawa and Y. Hashizume. An uncertainty analysis of temperature and velocity measured by a liquid crystal visualization technique. *Measurement Science and Technology*, 12:1235–1242, May 2001.

- [14] N. Fujisawa and R.J. Adrian. Three-dimensional temperature measurement in turbulent thermal convection by extended range scanning liquid crystal thermometry. *J. of Visualization*, 1:355–364, Feb 1999.
- [15] Gonzalez and Woods. *Digital Image Processing*. Addison-Wesley, first edition, 1992.
- [16] G.S. Grewal, M. Bharara, J.E. Cobb, V.N. Dubey, and D.J. Claremont. A novel approach to thermochromic liquid crystal calibration using neural networks. *Measurement Science and Technology*, 17:1918–1924, April 2006.